Nuclear Modification Factors and Identified Particle Ratios at BRAHMS in Cu+Cu collisions at $\sqrt{s_{NN}} = 200$ GeV

I C Arsene,[11] I G Bearden,[11] D Beavis,[11] S Bekele,[11] C Besliu,[11] B Budick,[11] H Bøoggild,[11] C Chasman,[11] C H Christensen,[11] P Christiansen,[11] H H Dalsgaard,[11] R Debbe,[11] J J Gaardhøje,[11] K Hagel,[11] H Ito,[11] A Jipa,[11] E B Johnson,[11] C E Jørgensen,[11] R Karabowicz,[11] N Katrynska,[11] E J Kim,[11] T M Larsen,[11] J H Lee,[11] G Løvhøiden,[11] Z Majeka,[11] M J Murray,[11] J Natowitz,[11] B S Nielsen,[11] C Nygaard,[11] D Pal,[11] A Qviller,[11] F Rami,[11] C Ristea,[11] O Ristea,[11] D Röhrich,[11] S J Sanders,[11] P Stazel,[11] T S Tveter,[11] F Videbæk,[11] R Wada,[11] H Yang,[11] Z Yin,[11] and I S Zugra[11]

[1] *Brookhaven National Laboratory, Upton, New York, USA*

[2] *Institut Pluridisciplinaire Hubert Curien et Universite Louis Pasteur, Strasbourg, France*

[3] *Institue of Space Science, Bucharest-Magurele, Romania*

[4] *M. Smoluchowski Inst. of Physics, Jagiellonian University, Krakow, Poland*

[5] *New York University, New York, USA*

[6] *Niels Bohr Institute, University of Copenhagen, Copenhagen, Denmark*

[7] *Texas A&M University, College Station, Texas, USA*

[8] *University of Bergen, Department of Physics and Technology, Bergen, Norway*

[9] *University of Bucharest, Romania*

[10] *The University Of Kansas, Lawrence, Kansas 66045*

[11] *University of Oslo, Department of Physics, Oslo, Norway*

(Dated: April 8, 2013)

We present results on identified particle spectra, nuclear modification factors(R_{AA}) and particle ratios at $y \sim 0$ and $y \sim 3$ for Cu+Cu collisions at $\sqrt{s_{NN}} = 200$ GeV. Kinetic freeze-out parameters of the Cu+Cu system are investigated as a function of centrality by a simultaneous blast-wave model fit to the pion, kaon and (anti)proton spectra. Particle yields, R_{AA}, and particle ratios are studied as a function of the number of participants to study how the heavy-ion reaction dynamics for a given number of participants depends on the overall system size. The Cu+Cu results are compared to data from lighter and heavier collision systems at the same RHIC energy to further unravel the dependence of physical observables on system size.

PACS numbers: 25.75.Gz

I. INTRODUCTION

Experiments at the Relativistic Heavy Ion Collider (RHIC)have been studying the properties of a deconfined state of matter created in collisions of heavy nuclei at very high energies. Originally predicted to be a weakly interacting gas of quarks and gluons (Quark Gluon Plasma, QGP in short)[1] which are collectively referred to as partons, the experimental evidence from RHIC compellingly pointed to the formation of a state of matter with properties characteristic of a nearly perfect liquid and which, accordingly, came to be known as strongly interacting Quark Gluon Plasma or sQGP in short [2]. As the QGP cools it undergoes a phase transition back to normal hadronic matter.

The matter created in heavy ion collisions exists for a very short period of time and its properties can be studied only indirectly through the measurment of hadrons, lep-

tons and photons. Hadrons from hard scattered partons are believed to probe the late stages of the dense medium while soft hadronic observables measure directly the final freeze-out stage of the collision. The early and dense stage of the collision can be directly studied through measurement of leptonic and electromagnetic observables. A major challenge in the field of relativisitic heavy ion collisions is then to find signatures that are unique to the QGP as opposed to properties of ordinary hadronic interactions.

It is expected that the signals from a deconfined phase should become stronger as the overlap region between the colliding nuclei increases. Investigating the difference between particle production in heavy ion collisions and elementary particle collisions is an important aspect of the research for the quest to understand the characteristics of the matter created in heavy ion collisions. Thus, the system size dependences of spectral shapes, hadron yields and their suppression, and particle ratios are some of the many observables that need to be studied in order to gain insight into the effect of the system size on the evolution of the matter created in the collisions. The measurement of the observables mentioned above in Au+Au collisions at $\sqrt{s_{NN}} = 200$ GeV has played a crucial role in characterizing the medium created in high-energy, nucleus-nucleus collisions. However, the study of the centrality dependence of these observables was limited to $N_{part} > 60$ leaving room for different scenarios of the N_{part} dependence of particle production in the large gap between the most peripheral Au+Au and p+p collisions. In order to extend the medium size dependence of physical observables down to small systems such as dAu and pp, the Cu+Cu system, with $A_{Cu} \sim 60$, was selected since it provides a good overlap with peripheral Au+Au in terms of the number of participants. Also, the relative uncertainity in the fractional cross-section of Cu+Cu collisions is smaller compared to that in Au+Au collisions for the same number of participants. The overlap region in central Cu+Cu is spherical while that in Au+Au for the same number of participants has an almond shape, making it possible to explore geometry effects on the experimental observables.

In this paper, we present transverse-momentum spectra, yields, $\langle p_T \rangle$, nuclear modification factor (R_{AA}) and ratios for identified charged hadrons ($\pi^{\pm}, K^{\pm}, p, \bar{p}$) based on transverse momentum spectra obtained with the BRAHMS spectrometeres in Cu+Cu collisions at $\sqrt{S_{NN}}$ = 200 GeV. The spectra are measured at two rapidities $y \sim 0$ and $y \sim 3$ as functions of collision centrality. The results will be compared to those obtained in pp and Au+Au collisions at the same energy, rapidity and centrality.

II. THE BRAHMS EXPERIMENT

The BRAHMS Experiment consists of two small acceptance magnetic spectrometers, the Mid-Rapidity Spectrometer (MRS) and the Forward Spectrometer(FS), for particle tracking and momentum determination and a system of global detectors made up of Beam-Beam Counters(BBC), Zero Degree Calorimeters (ZDC) and Multiplicity Arrays(MA) for event characterization[3]. The MRS uses two time projection chambers (TPCs), TPM1 and TPM2, with a magnet between them and time of flight (TOF) walls for particle identification (PID). The Forward Spectrometer (FS) has two TPCs(T1 and T2) and three Drift Chambers (DC) with magnets between consecutive detectors. In the FS, PID is achieved by using a TOF wall behind T2 and a second TOF wall and a Ring Imaging Cherenkov (RICH) detector after the third DC. The TPCs and DCs provide three dimensional space points which together with the momentum information provided by the magnets allow for particle tracking. The MRS is capable of rotating between 90° and 30° with respect to the beam pipe covering the rapidity interval from $y \sim 0$ to $y \sim 1.6$. The FS rotates between 15° and 2° and covers the rapidity interval from $y \sim 2.2$ to $y \sim 4.0$. For the data presented in this paper, the MRS

was set at 90° and the FS was set at 4°. The settings correspond to $y \sim 0$, $y \sim 3$ respectively.

A. Event Selection

The centrality of the collisions is characterized with a multiplicity array (MA) which consists of an inner array of Si strip detectors forming a hexagonal barrel surrounding the beam pipe where the interactions occur and an outer array of scintillator tile detectors also forming a hexagonal barrel coaxial with the inner strip detector system. By measuring the energy loss of charged particles that traverse the two arrays, the strip detectors and the tiles provide two semi-independent measurements from which the pseudo-rapidity dependence of the charged particle density can be deduced. A realistic GEANT simulation of the detector response is used in this determination to map energy loss to the corresponding number of primary particles. Reaction centrality is based on the distribution of integral particle densities with the nominal pseudorapidity range covered by the MA of $-2.2 < \eta < 2.2$, with the centrality of a given event taken as a fraction of observed events with a greater integral density to the total number of events using the HIJING model to estimate the number of events missed because they do not leave sufficient energy in the MA for detection.

The primary collision vertex position is determined to an accuracy of ∼1 cm based on the relative time-of-flight of fast ($\beta \approx 1$) particles hitting beam-beam counter arrays (BBCs). The BBCs consist of Cherenkov detectors mounted on photomultiplier tubes and are located 220 cm on either side of the interaction region. The BBCs also provide the start time for the time of flight (TOF) measurements.

For this analysis, the events have been divided into four centrality classes ($0-10\%, 10-30\%, 30-50\%$ and $50-70\%$). Events within ±25 cm of the nominal vertex were selected. Since the spectrometer acceptance varies from one event to another due to changing vertex location, spectral analysis is carried out in vertex bins of 5 cm and the results are statistically averaged to obtain a final spectra.

B. Track Selection

Straight line track segments are determined by tracking detectors which are outside the magnetic field regions. Matching track segments across the analyzing magnets make it possible to determine the momentum associated with the matched tracks from the vertical magnetic field, the length traversed in the magnetic field region, the polar angle of the tracks with respect to the matching plane, and the average vertical slope of the tracks. The matching plane is defined as the vertical plane that contains the perpendicular bisector of the line joining the effective edge entry and exit points of the tracks. Once the momentum is known,the reconstructed tracks are projected toward the beam axis and checked for consistency with the collision vertex determined by the BBCs. A 3σ cut is applied about the mean of the distribution of differences between the projected track vertex and the BB vertex along the beam direction . An elliptical cut of 3σ is applied to the x,y distributions of track intersections with the primary vertex plane defined as the plane normal to the beam axis and containing the collision vertex. The rapidity cuts were $|y| < 0.1$ at mid-rapidity and $2.95 < y < 3.15$ at forward rapidity.

C. Particle Identification

In this analysis , the MRS time of flight (TOFW) and the FS RICH detectors have been used for PID at y = 0 and y = 3 respectively. The time of flight measurement with TOFW and knowledge of the flight path length allows one to determine β, which together with the momentum of a detected particle provides for particle identification according to the relation given by

$$\frac{1}{\beta^2} = \frac{m^2}{p^2} + 1 \ . \tag{1}$$

Particles of different masses fall on separate curves if $\frac{1}{\beta}$ is plotted versus momentum. The TOFW provides π/K separation up to a momentum of 2 GeV/c and K/p separation up to 3 GeV/c.

For the FS, the emission angle θ_c of the light cone radiated in the RICH detector along the particle path is constant and is given by

$$\cos\theta_c = \frac{1}{n\beta}, \tag{2}$$

where n is the index of refraction of the gas inside the RICH volume. The particle detection is based on the focusing of light cones onto rings whose radii are related to θ_c and the focal length L of the spherical mirror used to focus the light, with

$$\theta_c = \tan^{-1}(\frac{r}{L}). \tag{3}$$

Once the radii of the rings are measured, PID is done in accordance with the formula

$$r = L\tan\ [\cos^{-1}(\ \frac{1}{n}\sqrt{1+\frac{m^2}{p^2}}\ )\ ]. \tag{4}$$

The RICH can identify pions starting at 2.5 GeV/c, kaons starting around 8 GeV/c and protons(anti-protons) from 15 GeV/c. π/K separation extends up to 20 GeV/c and protons(anti-protons) can be identified up to 35 GeV/c. Figure 1 (top) shows the distribution of $\frac{1}{\beta}$ *vs.* p for the MRS where $q = 1$ for positive particles and $q = -1$ for negative particles. Figure 1(bottom) shows the distribution of radius r *vs.* p for the RICH. The curves show the 3σ cuts around the nominal trajectories for the different particle species. For this analysis, tracks were required to have measured $\frac{1}{\beta}$ values within 3σ of the nominal values given by Eq.(1) at y= 0 for each particle species. At y = 3, the tracks were required to have a RICH radius within 3σ of the nominal radius determined from Eqn. (4).

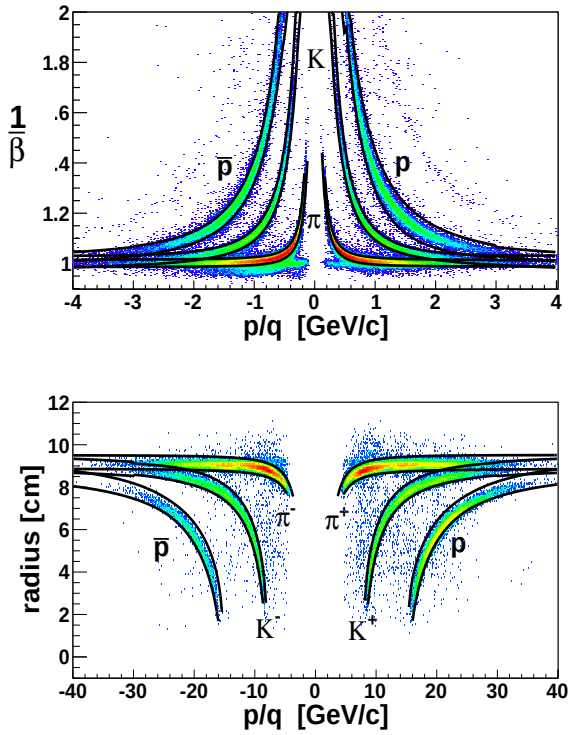

FIG. 1. $\frac{1}{\beta}$ versus p distribution (top) and Radius versus p (bottom). The solid curves show the 3σ cut around the nominal values given by Eqn.(1) and Eqn.(4).

D. Corrections

The data presented here have been corrected for the geometrical acceptance of the spectrometers, tracking efficency, particle mis-identification and the effects of particle decays. The BRAHMS detector response is modeled using a realistic GEANT simulation of the experimental arrangement. This simulation is used to correct the experimental results for effects such as interactions with the beam pipe, absorption, and multiple scattering within the gas volumes of the tracking detectors.

The geometrical acceptance is accounted for using the GEANT Monte-Carlo simulations. Particles are "thrown" with a uniform momentum distribution over a range of angles $\Delta\phi$ and $\Delta\theta$ broad enough for the spec-

trometer aperture to lie within the range. The acceptance factor for a given pseudorapidity range is then the fraction of accepted particles to those thrown scaled by $\frac{\Delta\phi}{2\pi}$. This is done for each vertex bin and the different spectrometer angle and magnetic field settings. The acceptance correction is applied to the individual spectra for the difference spectrometer settings before they are averaged.

The tracking efficiency is calculated using the reference track method where good tracks from one detector are taken as input to a detector whose efficiency is sought. For the MRS, for example, tracks from the first time projection chamber (TPC) are used as input to determine the efficiency for the second TPC, and vice-versa. The ratio of the number of tracks matching the reference tracks to the total number of input reference tracks is taken as the tracking efficiency. The product of the efficiencies calculated for the two MRS TPC's in this way is then taken to be the overall tracking efficiency for the MRS and is $\sim 92\%$. For the FS, the overall tracking efficiency is $\sim 80\%$. The systematic uncertainty associated with the determination of the tracking efficiency is $\sim 5-8\%$. The tracking efficiency is applied to the final MRS spectra. For the FS the efficiency correction was applied on a track by track basis.

To determine the GEANT based corrections, single particle events were processed through the standard BRAHMS analysis code. The simulations included multiple scattering and hadronic interaction processes. The GEANT corrections are applied on a track by track basis for both the MRS and FS.

To take into account particle mis-identification, a pid correction has been applied to the pion and kaon spectra for $p > 1.5$ GeV/c(MRS) and $p > 20$ GeV/c(FS). The systematic uncertainities on the pid corrections have been estimated by studying the distributions of M^2 *vs.* p(MRS and FS), $\frac{1}{\beta}$ *vs.* p(MRS),and r *vs.* p(FS). For the pions at $y \sim 0$, the pid correction is $< 1\%$ at $p \sim 1.5$ GeV/c and increases to about 15% at $p \sim 2.25$ GeV/c with a systematic uncertainity of less than 1%. For the kaons, the corrections vary between 1% at $p \sim 1.5$ GeV/c with $< 0.5\%$ systematic uncertainty and $\sim 50\%$ at $p \sim 2.25$ GeV/c where the systematic uncertainty is $\sim 5\%$. For the pions at $y \sim 3$, the pid correction is $< 1\%$ at $p \sim 24$ GeV/c with a systematic uncertainity of less than 1%. The correction increases to $\sim 12\%$ at $p \sim 30$ GeV/c with a systematic uncertainity of $\sim 5\%$. For the kaons, the pid correction is $< 1\%$ at $p \sim 24$ GeV/c with a systematic uncertainity of less than 1%. The correction increases to about $\sim 25-30\%$ at $p \sim 30$ GeV/c with a systematic uncertainity of $\sim 5\%$. In the momentum range covered, the (anti)protons are well separated from the mesons and no pid correction is applied to their spectra.

III. RESULTS AND DISCUSSION

A. Identified particle spectra

Measurement of transverse momenta is the crucial first step in obtaining the various observables used to characterize the properties of the partonic medium created in heavy ion collisions. Figure 2 shows the invariant spectra for the charged hadrons $\pi^{\pm}, K^{\pm}, p$ and $\bar{p}$, versus transverse kinetic energy, for different collision centralities at $y \sim 0$ and $y \sim 3$. The spectra of particles and antiparticles have very similar shapes. Comparing pions, kaons and protons we see a steady hardening of the spectra with particle mass. Both of these effects are suggestive of hydrodynamics. The lines in Fig. 2 are fits of the hydrodynamically inspired Blast Wave model [6] to the six $\pi^{\pm}, K^{\pm}, p$ and $\bar{p}$ spectra at a given rapidity and centrality. These fits will be discussed in detail later. The magnitude of the spectra depend strongly on centrality for all particles and both rapidities. For kaons and protons the shape of the spectra harden as one moves from peripheral to central collisions. It is clear that the spectra of all particles are softer at forward rapidity but otherwise

the trends observed with particle mass and centrality are similar at both rapidities.

We have done a systematic study of the spectra by fitting them to a variety of functions. The resulting fitting parameters, χ^2 per degree of freedom, $\frac{dN}{dy}$, and $\langle p_T \rangle$ are listed in Tables IV V, and VI. For pions exponential functions in transverse momentum p_T ($Ae^{-\frac{p_T}{T}}$), transverse mass $m_T = \sqrt{m^2 + p^2}$ ($Ae^{-\frac{m_T}{T}}$), and a power law function $A(1 + \frac{p_T}{p_o})^{-n}$ where able to fit the data. The kaon spectra can be reasonably fit using exponentials in p_T, m_T or a Boltzmann function m_T ($Am_T e^{-\frac{m_T}{T}}$). For protons and antiprotons only exponentials in m_T and Boltzmann functions could describe the spectra.

For the pions, exponentials in p_T and m_T give similar results while the power law function results in larger values of $\frac{dN}{dy}$ and smaller values of $\langle p_T \rangle$. The power law function gives the best description of the pion data at central rapidity with χ^2/NDF much lower than for the exponential functions. At forward rapidity the χ^2/NDF values are similar for each of the three functional forms.

For the kaons, $(\frac{dN}{dy})_{p_T\ Exp.} > (\frac{dN}{dy})_{m_T\ Exp.} > (\frac{dN}{dy})_{m_T\ Boltz.}$ and $\langle p_T \rangle_{p_T\ Exp.} > \langle p_T \rangle_{m_T\ Exp.} > \langle p_T \rangle_{m_T Boltz.}$. The range of values for χ^2/NDF are similar for all three functions at both central and forward rapidity. For the protons and anti-protons, both the m_T exponential and the Boltzmann function give similar results for $\frac{dN}{dy}$ but $\langle p_T \rangle_{m_T\ Exp.} > \langle p_T \rangle_{m_T\ Boltz.}$. Both functional forms have similar χ^2/NDF values.

A model dependent analysis of the transverse momentum spectra as a function of rapidity and centrality allows one to extract the thermodynamic and collective properties of the system at kinetic freeze-out. Considering the large collective flow observed at RHIC and in order to gain more insight into the evolution of the kinetic freeze-out parameters, we have studied the identified particle spectra using a hydro-inspired blast wave model [6]. At mid-rapidity, the model predicts a spectrum in m_T with

$$\frac{dN}{m_T dm_T} \sim \int_0^{R_{max}} dr\ \{r \times n(r) \times [m_T I_0(x) K_1(z)]\} \quad (5)$$

where $x = \frac{p_T}{T}\sinh(\rho)$, $z = \frac{m_T}{T}\cosh(\rho)$, $\rho = tan^{-1}(\beta_T)$, and $\beta_T(r) = \beta_s(\frac{r}{R})^\alpha$ is the velocity profile with $\frac{r}{R}$ accounting for the change in the velocity as a function of radial distance. In Eqn. 6, $n(r)$ is the radial density profile which is equal to 1 for a box profile for $0 < r < R_{max}$ and zero otherwise. For this analysis, $n(r)$ is assumed to have a Gaussian form $\sim e^{\frac{r^2}{2R^2}}$ with R representing the width of the Gaussian and $R_{max} = 3R$. While β_s corresponds to a surface velocity in the case of a box density profile, it is considered as a fit parameter for the Gaussian profile. The modified Bessel function $K_1(z)$ comes from integration from $-\infty$ to $+\infty$ over pseudorapidity η assuming boost invariance. At forward rapidity, the assumption of boost invariance is not valid and $K_1(z)$ should be replaced by integration over η over a finite range so that

$$\frac{dN}{dy m_T dm_T} \sim \int_0^{R_{max}} dr\ \{r \times n(r) \times [m_T I_0(x) g(z)]\} \quad (6)$$

where

$$g(z) = \int_{\eta_{min}}^{\eta_{max}} \cosh(\eta - y)\ e^{-z\cosh(\eta - y)}\ d\eta \quad (7)$$

and y is the rapidity variable. The integration in Eqn. (7) was carried out, with $y = 3$, over 2 units of pseudorapidity from $\eta_{min} = 2.4$ and $\eta_{max} = 4.4$. For both the mid-rapidity and forward-rapidity data, we performed a simultaneous fit of the pion, kaon and (anti)proton spectra with 3 parameters: T, β_s, and α. The normalization parameters can be calculated from the data using expressions obtained from the χ^2 minimization. Feed down from resonances was not considered as there are no Cu+Cu data below 0.4 GeV/c. The fit range is restricted to $p_T < 1.8$ GeV/c for pions, $p_T < 2.0$ GeV/c for kaons since hard processes are expected to become sig-

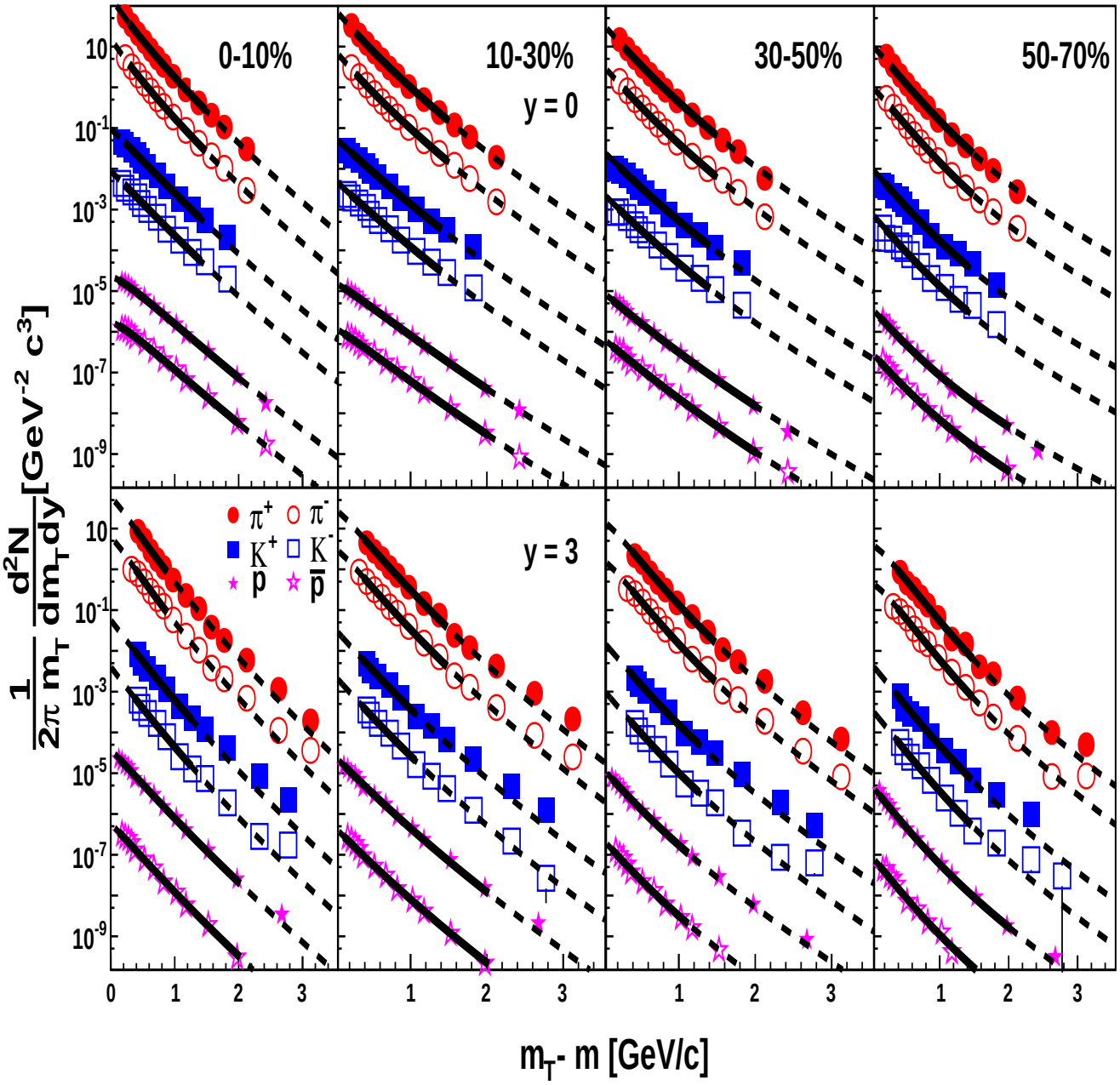

FIG. 2. Invariant spectra versus transverse kinetic energy at $y \sim 0$ (top panels) and $y \sim 3$ (bottom panels) as a function of centrality for $\pi^{\pm}, k^{\pm}, p$, and $\bar{p}$. The π^-, k^+, k^-, p and $\bar{p}$ spectra are scaled by factors of $10^{-1}, 10^{-2}, 10^{-3}, 10^{-4}$, and 10^{-5} respectively. The lines show the results of blast wave fits to each of the six spectra at a given rapidity and centrality. The solid lines indicate the fit range used while the dashed lines are extrapolations beyond the fit range. Only statistical errors are shown

nificant above these momenta, and $p_T < 3.0$ GeV/c for (anti)protons. For the forward rapidity data, the forward spectrometer setting at 4° corresponds to $\eta = 3.4$.

The fit results are presented in Figure 3. The fit parameters T_{kin} and β_s are given in Table I. In Figure 2, the lines are fits to blast wave model with the solid lines indicating the transverse mass (or momentum) range for the fits and the dotted lines are extrapolations using the extracted fit parameters.

Figure 4 shows the centrality dependence of the effec-

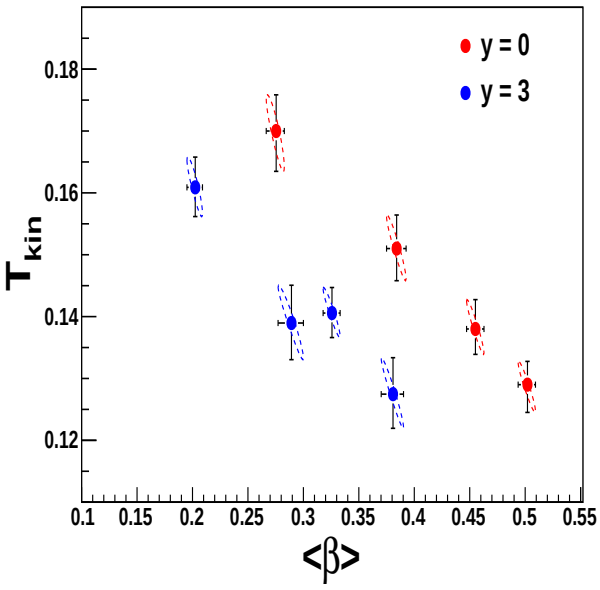

FIG. 3. T_{kin} vs. β_s for a fixed value of α. Centrality increases to the right.

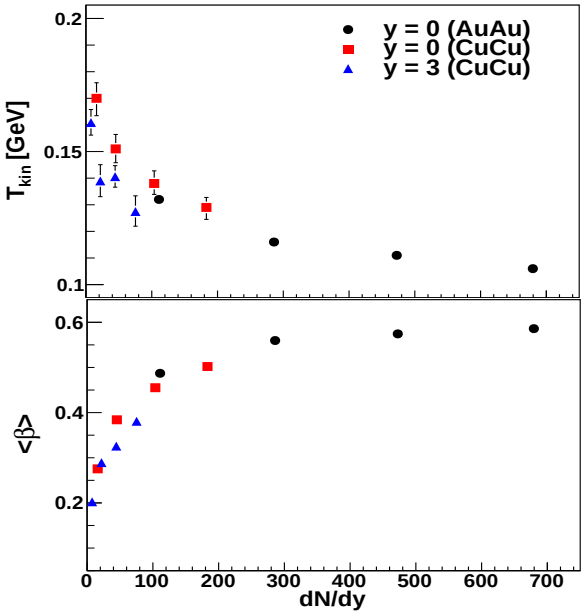

FIG. 4. T and $\langle\beta\rangle$ as a function of $\frac{dN}{dy}$.

tive temperature and the mean radial flow velocity. We observe that the temperature decreases while the flow velocity increases going from peripheral to central collisions. This can be understood from the perspective of energy conservation where the decrease in temperature shows up as an increase in kinetic energy due to the radial flow. We also notice that the flow velocity is smaller at y = 3 compared to that at y = 0. This may be a consequence of the fact that the system has a smaller size at y = 3 with less number of particles to interact with each other.

$Cent.$	$T_{kin}(MeV)$	$\langle\beta\rangle$	α	χ^2/dof
	$y=0$			
$0-10\%$	129 ± 1	0.502 ± 0.002	0.494 ± 0.002	0.83
$10-30\%$	138 ± 1	0.455 ± 0.002	0.599 ± 0.004	0.98
$30-50\%$	151 ± 2	0.384 ± 0.004	0.786 ± 0.073	0.94
$50-70\%$	170 ± 4	0.275 ± 0.007	1.28 ± 0.19	1.0
	$y=3$			
$0-10\%$	128 ± 4	$.378\pm0.029$	0.738 ± 0.193	0.99
$10-30\%$	142 ± 5	$.321\pm0.030$	0.905 ± 0.099	1.04
$30-50\%$	141 ± 6	$.289\pm0.034$	1.08 ± 0.11	1.00
$50-70\%$	160 ± 8	$.203\pm0.060$	1.534 ± 0.033	1.00

TABLE I. T_{kin}, $\langle\beta_T\rangle$,and α for identified charged hadrons.

The integrated yields are obtained by extrapolating outside the measurement region. The faction of the particle yield within the BRAHMS acceptance varies from $30-75\%$ depending upon the spectrometer setting used. The $\frac{dN}{dy}$, $\langle p_T\rangle$, and fraction of particles in the BRAHMS acceptance are summarized in Tables II, III. We note that the results from the blast wave fit are in reasonable agreement with the results obtained by fitting the data to the simple functions discussed above.

The dN/dy scaled by N_{part} are shown in Figure 5 at mid (left) and forward (right) rapidities respectively. The corresponding $\langle p_T\rangle$ versus N_{part} are shown in Fig. 6. The scaled dN/dy and $\langle p_T\rangle$ for the pions and kaons from $Cu+Cu$ join smoothly with those from $Au+Au$ at $\sqrt{s_{NN}}=200$ GeV, except for a slight excess of kaons and deficit of pions for CuCu near $N_{part}\sim 50$. The (anti)protons at $y=0$ are corrected for contributions from Λ decays. The data show a slight centrality dependence of the scaled dN/dy at both rapidities. While the the pion $\langle p_T\rangle$ at y = 3 is similar to that at y = 0, the kaons and (anti)protons exhibit smaller values. The pion $\langle p_T\rangle$ appears to be independent of centrality, while the

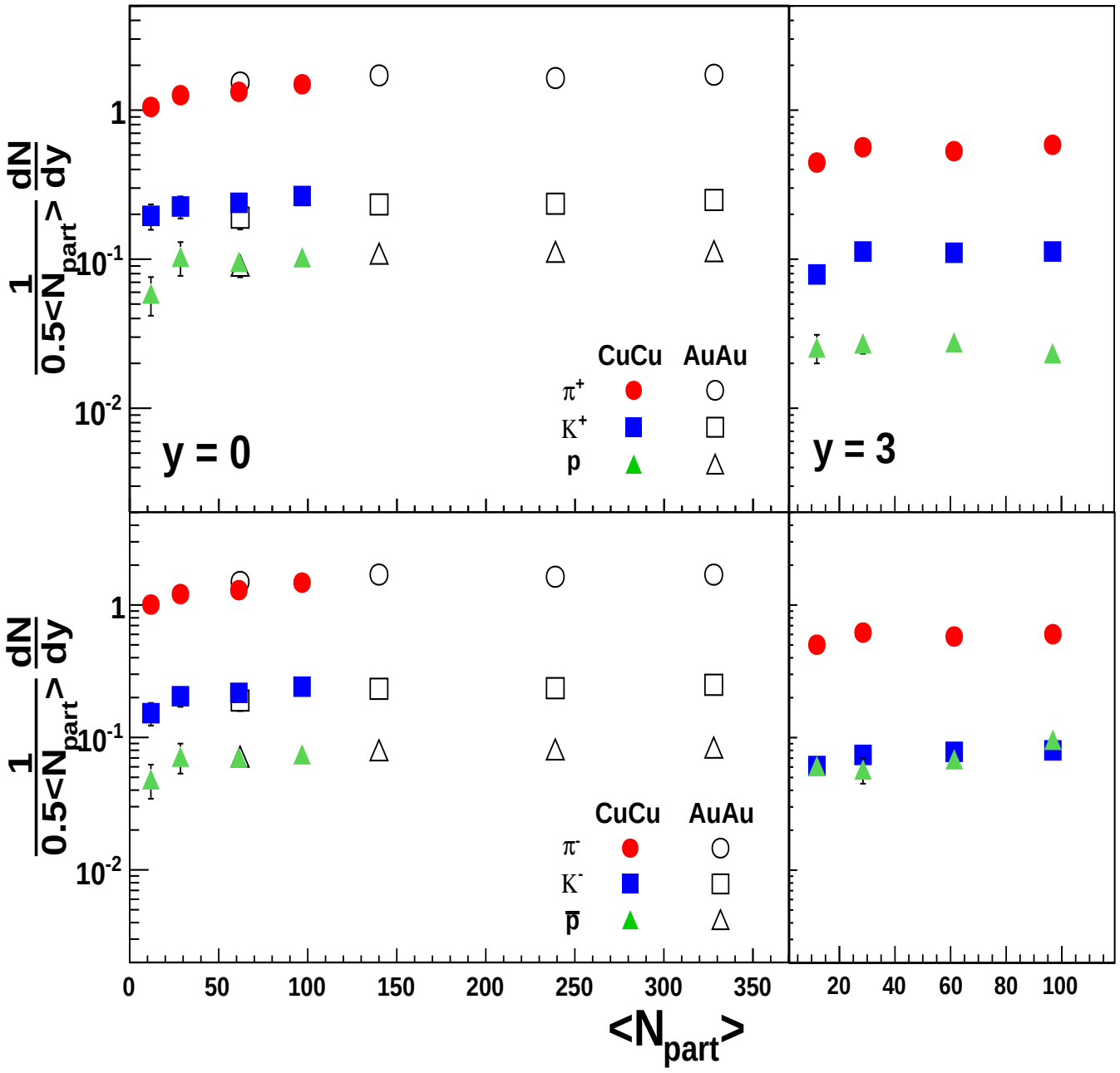

FIG. 5. N_{part} scaled $\frac{dN}{dy}$ as a function of centrality at $y \sim 0$

kaon and the (anti)proton $\langle p_T \rangle$ increases from peripheral to central $Cu + Cu$ collisions at mid-rapidity. The pions and kaons show no dependence on centrality at forward rapidity while the (anti)proton $\langle p_T \rangle$ appears to increase with centrality. One can see that $\langle p_T \rangle$ increases with the particle mass indicating the heavier particles are more affected by radial flow than the lighter particles. The fact that the Cu+Cu data points join smoothly with those from Au+Au collisions indicates that the size of the colliding system does not matter as most physical observables turn out to be the same for the same number of participants. This also suggests that the data are insensitive to the difference in geometry of the Cu+Cu and Au+Au overlap regions for the same number of partici-

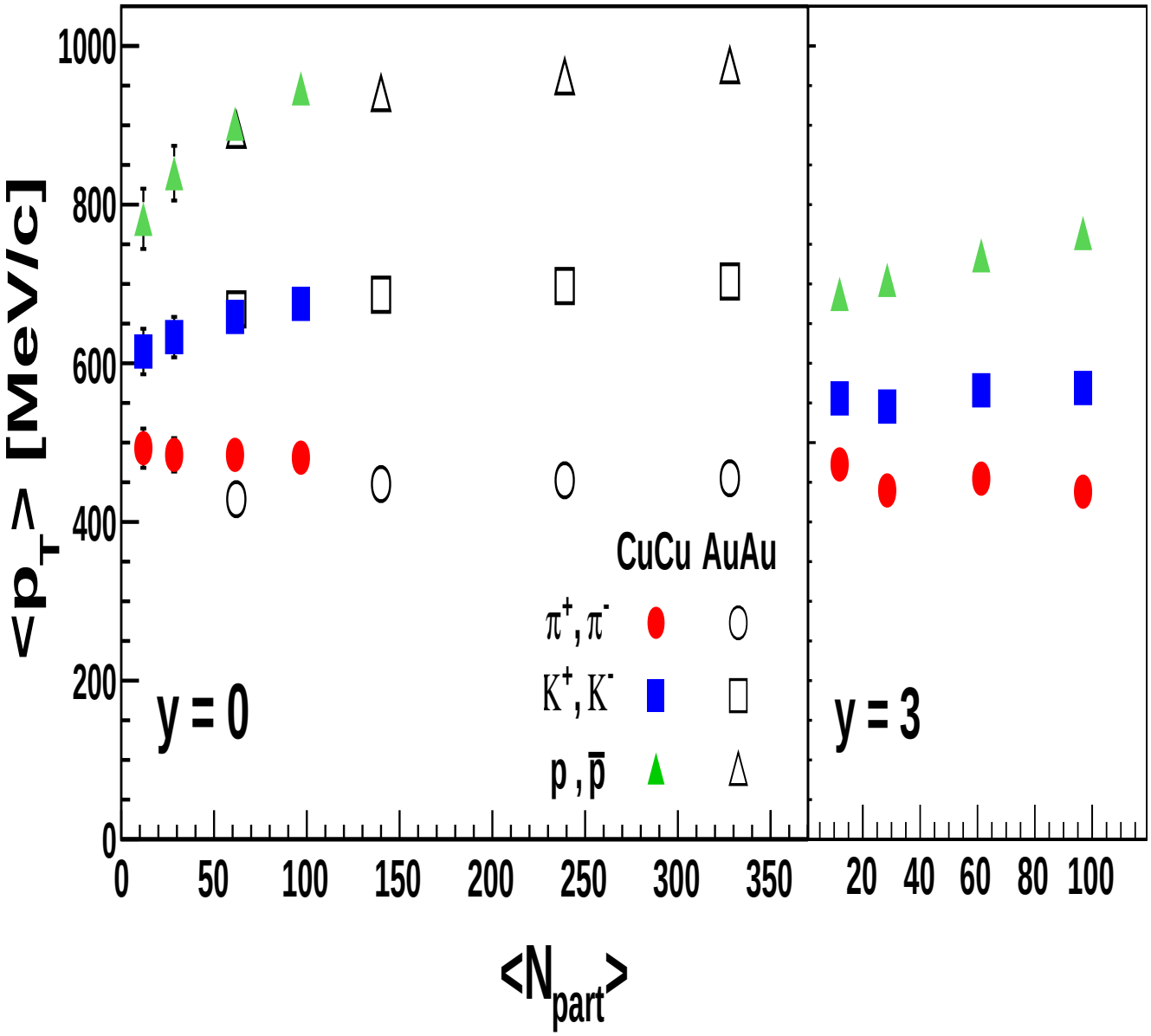

FIG. 6. Mean p_T as a function of centrality at $y \sim 0$

pants.

B. Nuclear Modification Factors

The discovery of hadron suppression in heavy ion collisions at RHIC has been one of the most exciting results [7]. In central heavy ion collisions, suppression of hadrons at mid-rapidity is believed to be a consequence of the energy loss of partons in the dense medium formed in the collisions. Such a suppression was observed in central Au+Au collisions at RHIC. The origin of the suppression at forward rapidity observed in 200 GeV d+Au and Au+Au collisions is not yet very well understood. Significant theoretical effort is being devoted to understand the

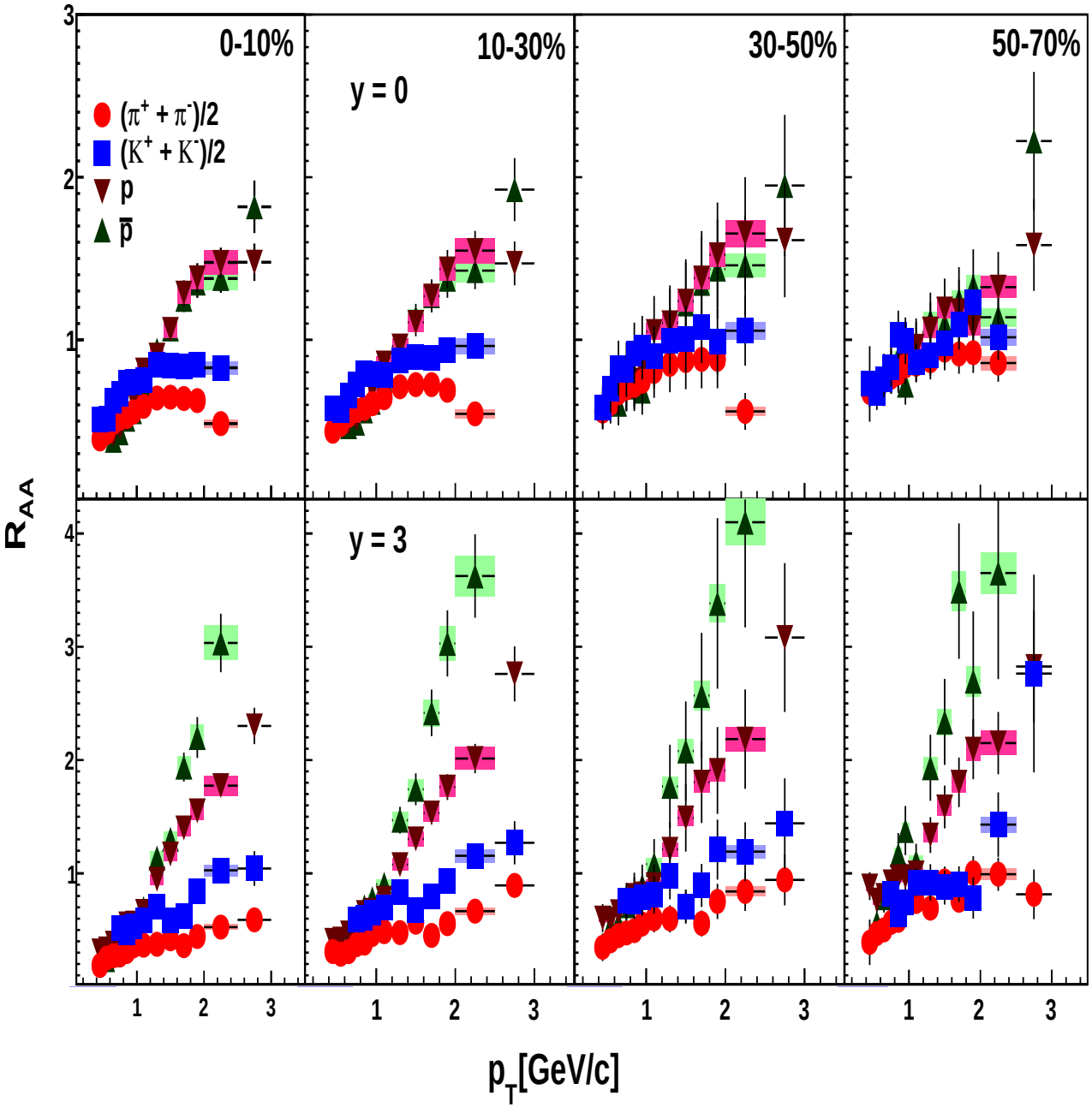

FIG. 7. Nuclear modification factor for kaons

roles of final state and initial state interactions on particle production as a function of transverse momentum, rapidity and centrality [8–10]. The effect of the medium on particle production is studied in terms of the nuclear modification factor R_{AA} defined as

$$R_{AA} = \frac{d^2N_{AA}/dp_T dy}{\langle N_{bin}\rangle d^2N_{pp}/dp_T dy} \tag{8}$$

which is the ratio of the particle yield in heavy ion collisions to the yield in pp collisions scaled by the average number of binary collisons N_{bin} with in a heavy ion collision. At low p_T, R_{AA} approaches the value of $\frac{N_{part}/2}{N_{bin}}$. If AA collisions were just a superposition of elementary collisions between nucleons, then $R_{AA} \to 1$ at high p_T.

Figure 7 shows the nuclear modification factor R_{AA}

for pions, kaons and (anti)protons respectively in Cu+Cu collisions. The pion and kaon R_{AA} are averages of the positive and negative particles. The Pion data above $p_T > 1$ GeV/c show that the suppression decreases in going to more peripheral events. This is consistent with the fact that the multiplicity density decreases as one goes to more peripheral colliions; there is less matter to interact with and more pions make it out of the collision region before losing much of their energy. The kaon R_{AA} shows a slightly smaller level of suppression as that of the pions and similar dependence on centrality. No suppression is found for (anti)protons at $y \sim 0$. At mid-rapidity, the R_{AA}-values above 1.5 GeV/c seems to be constant with increasing p_T for all particle types and centralities.

The significant suppression of pions and kaons in the p_T range covered by the BRAHMS results suggests that the effect of energy loss may extend to as low as 1.5 GeV/c in p_T which is quite removed from the hard processes regime ($p_T > 6$ GeV/c). At mid-rapidity, the baryons are not suppressed above 1.5 GeV/c for any centrality range. The baryons at forward rapidity, on the other hand, show a significant enhancement with $R_{AA} > 1$ for all centrality classes, with the anti protons having the larger enhancement.

C. Particle Ratios

Figure 8 shows antiparticle to particle $\frac{dN}{dy}$ ratios measured in Cu+Cu collisions at $\sqrt{s_{NN}} = 200$ GeV/c as a function of the number of participants, N_{part}. The left panel is for $y \sim 0$ and the right panel for $y \sim 3$. These ratios of integrated yields do not exhibit a centrality dependence at mid-rapidity. At r $y \sim 3$ there is a slight drop of the $\frac{\pi^-}{\pi^+}$ ratio with centrality.

Figure 9 shows the kaon to pion ratios (upper two panels) and baryon to meson ratios (lower two panels) as functions of p_T, centrality and rapidity. At mid-rapidity, the data show a linear increase at low p_T but seem to saturate for $p_T > 1.5$ GeV/c,with the $\frac{K^+}{\pi^+}$ ratio showing only a slight excess over the corresponding $\frac{K^-}{\pi^-}$ values. At $y \sim 3$ the $\frac{K^+}{\pi^+}$ shows some centrality dependence and is significantly enhanced over the corresponding $\frac{K^-}{\pi^-}$ results.

The N_{part} dependence of the $\frac{K}{\pi}$ ratios are displayed in Figure 10 where the data have been integrated over $1.3 < p_T < 2.0$ GeV/c for $y \sim 0$ and over $1.5 < p_T < 3.0$ GeV/c for $y \sim 3$. The $\frac{K}{\pi}$ ratio shows a dependence on centrality at mid rapidity, but this ratio seems to saturate at forward rapidity for mid-central to central events. The greater $\frac{K^+}{\pi^+}$ values as compared to the $\frac{K^-}{\pi^-}$ results may be attributed to the larger baryon density which increases the probability of associated production for K^+. At $N_{part} \sim 50$ the integrated $\frac{K^\pm}{\pi^\pm}$ ratios in Cu+Cu collisions are higher than those observed in Au+Au collisions for similar values of N_{part}, see Fig. 5. This is similar to an observation by the STAR collaboration that the yield of strange mesons and baryons rises more quickly with N_{part} in Cu+Cu collisions compared to Au+Au [22].

An enhancement of baryons over mesons is observed at both rapidities. It has been shown before that the $\frac{p}{\pi}$ ratio at mid-rapidity approaches unity, contrary to what is observed in elementary particle collisions where the ratio does not exceed 0.2 in the corresponding momentum range for both quark and gluon jets. The fact that the $\frac{p}{\pi^+}$ and $\frac{\bar{p}}{\pi^-}$ ratios are close to unity in the intermediate p_T region for central collisions may be attributed to either quark coalescence [8] or baryon transport dynamics based on topological gluon field configurations [12].

The dependence of the baryon to meson ratios on N_{part} are displayed in Figure 10. The ratios seem to exhibit a monotonic increase with N_{part}. At mid-rapidity is, the ratios are smaller than unity with $\frac{p}{\pi^+}$ values larger than the corresponding $\frac{\bar{p}}{\pi^-}$ values. At forward rapidity, the $\frac{p}{\pi^+}$ ratio is generally greater than unity and is larger than the corresponding $\frac{\bar{p}}{\pi^-}$ ratio by almost a factor of 6. This has also been observed in Au+Au collisions at the same energy. While the beam protons may be contributing to the $\frac{p}{\pi^+}$ ratio, the reason for such large difference between

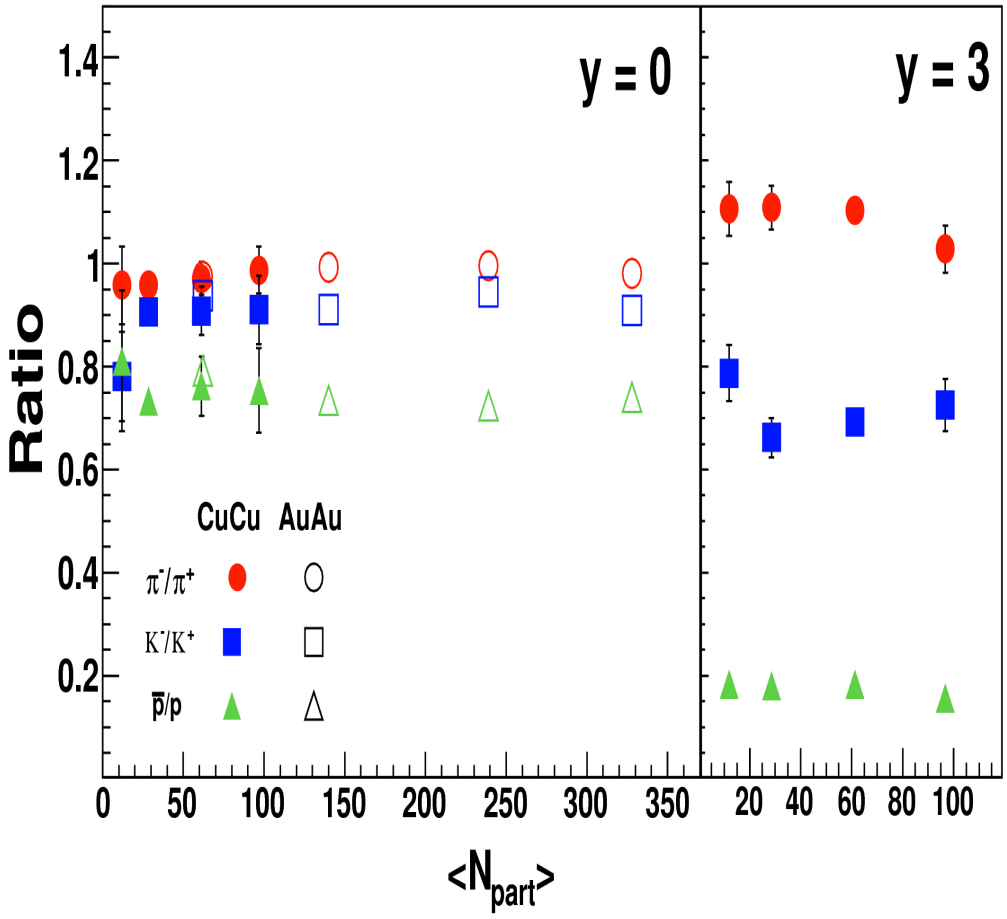

FIG. 8. Like particle ratios versus N_{part} for identified particles

the positive and negative baryon to meson ratios is not yet well understood. At both $y \sim 0$ and $y \sim 3$, there appears to be a centrality dependence of the baryon to meson ratio with the ratio decreasing going from central to peripheral collisions. This is unexpected considering that baryons are supposed to come from gluons and pions from quarks. Due to their large couplings gluons lose more energy than quarks resulting in a reduced production of baryons compared to pions. As a result one expects the $\frac{\bar{p}}{\pi^-}$ ratio to be lower in central Cu+Cu collisions than in peripheral collisions, which is opposite to what is observed. The results are consistent with the observation that the R_{AA} values indicate mesons become more suppressed for central events, while R_{AA} values for

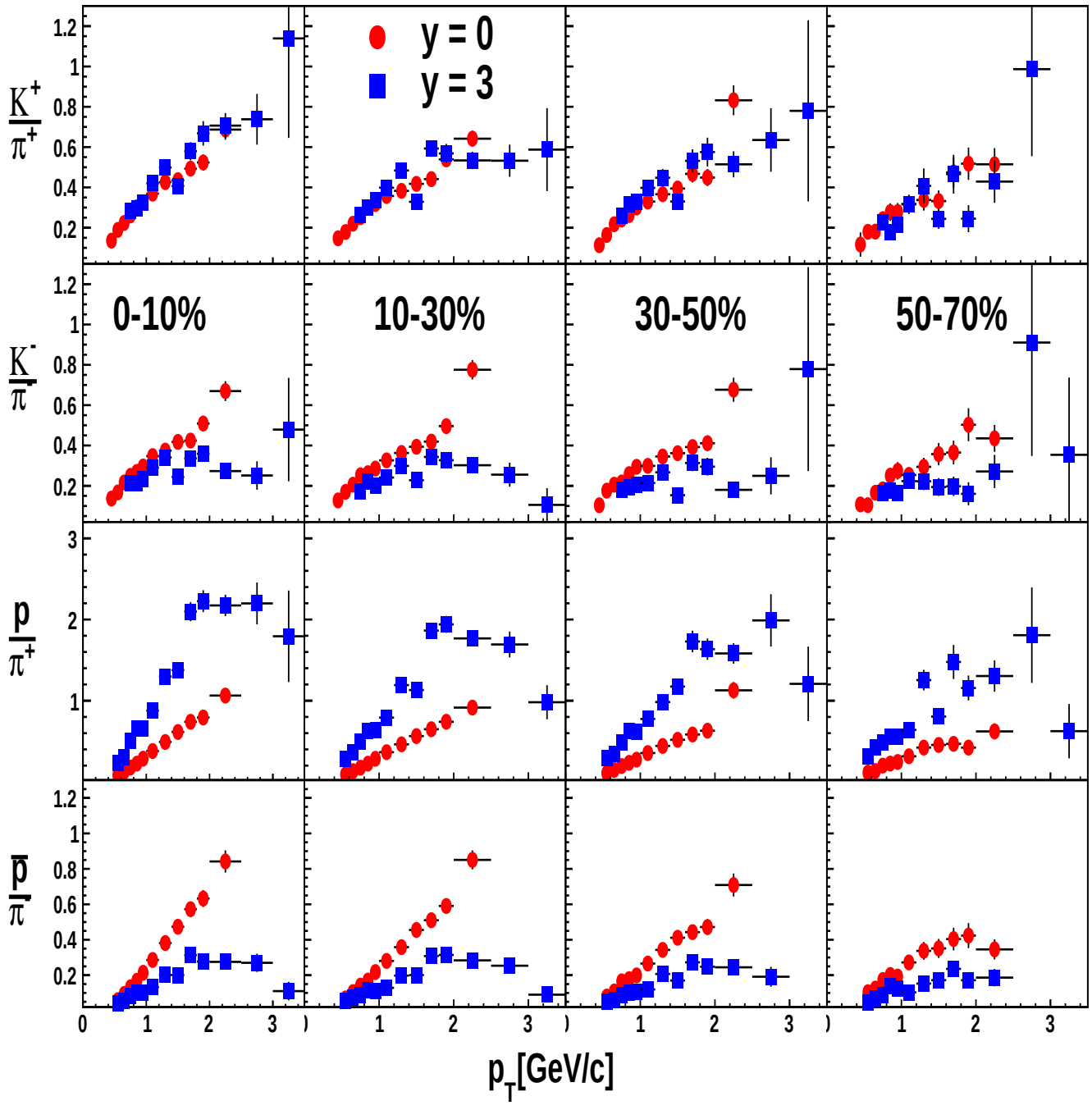

FIG. 9. Particle ratios as a function of $\langle p_T \rangle$, at $y \sim 0$ (circle) and $y \sim 3$ (square).

baryons show little centrality dependence.

IV. CONCLUSIONS

BRAHMS has measured transverse-momentum spectra, yields and ratios for identified charged hadrons ($\pi^{\pm}, K^{\pm}, p, \bar{p}$ in 200 GeV Cu+Cu collisions at two rapidities $y = 0$ and $y \sim 3$ as a function of collision centrality. Following the assumption that a thermally equilibrated flowing bulk medium can be described within the framework of the hydrodynamic model, a simultaneous blast wave fit to the data was used to extract the kinetic freeze-out parameters T_{kin}, $\langle \beta \rangle$, the scaled dN/dy and $\langle p_T \rangle$. The results obtained at mid-rapidity are found to

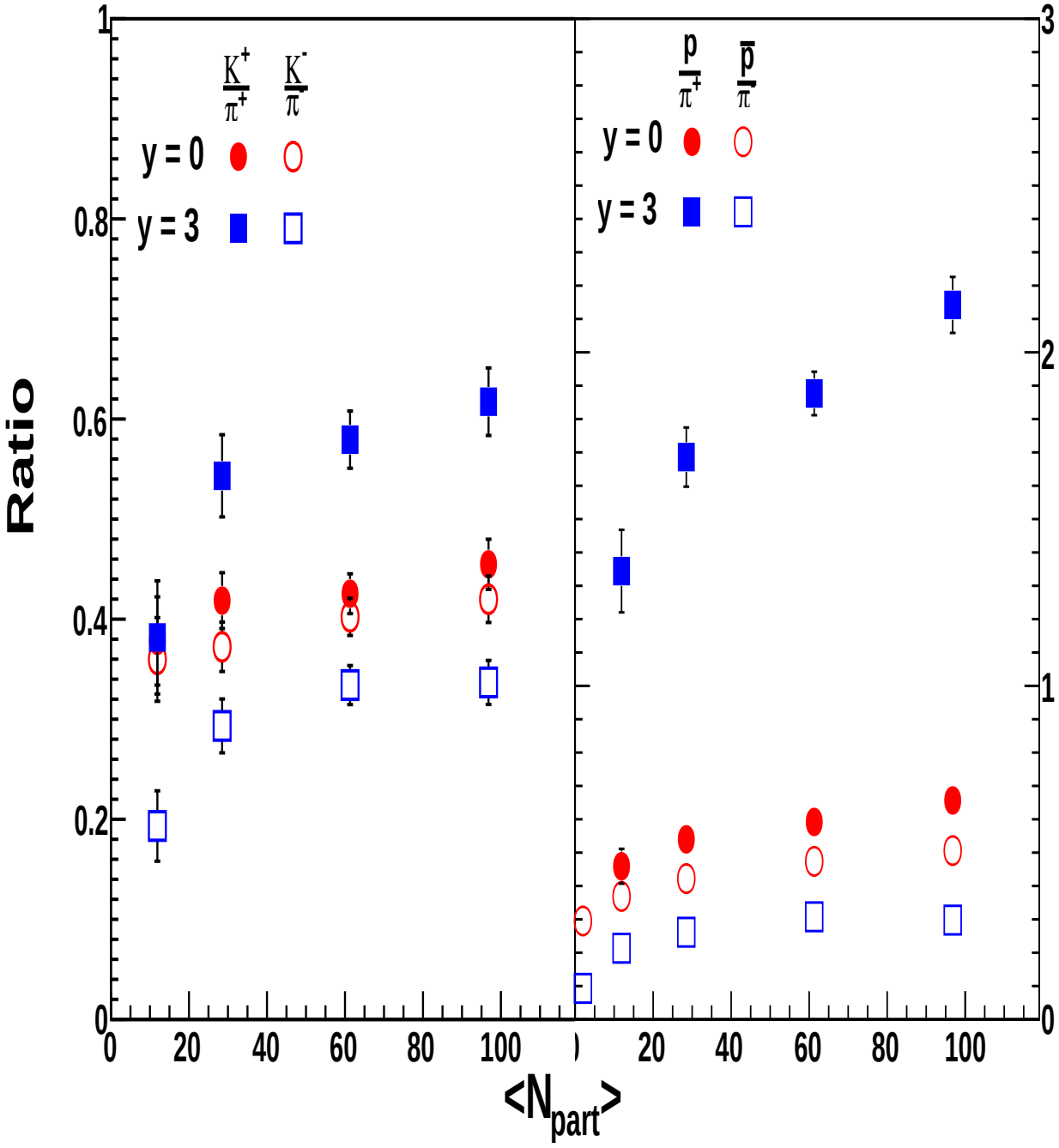

FIG. 10. $\frac{K}{\pi}$(left) and Baryon to meson(right) ratios as a function of N_{part}, at $y \sim 0$ and $y \sim 3$.

be similar to those in Au+Au for the same number of participants indicating that the geometry of the overlap zone does not significantly affect the particle spectra. It would be interesting to see if the similarity between Cu+Cu and Au+Au results for the same number of participants persists at forward rapidities. At forward rapidity, there seems to be no dependence of the freeze-out parameters on the size of the overlap zone.

Pions and kaons exhibit similar levels of suppression with the suppression decreasing going to peripheral collisions. The baryons are not suppressed and show no centrality dependence at mid-rapidity. Even though the particle density gets smaller at forward rapidities, the meson suppression pattern remains similar to what is ob-

served at mid rapidity. At forward rapidity the baryons again show little centrality dependence although with the anti-protons showing a bigger enhancement.

The BRAHMS Cu+Cu data essentially covers the intermediate p_T region ($2 < p_T < 5$ GeV/c) which is expected to be influenced by the interplay between fragmentation and recombination,i.e., the fragmentation process may be altered by the surrounding environment [13]. The significant meson suppression in this p_T region measured by BRAHMS can be used to test parton fragmentation + recombination/coalescence [8, 14] models which have been found to describe very well particle production in the intermediate p_T region. At RHIC energies, hard parton scattering has been found to dominate the spectrum at high p_T ($p_T > 6$ GeV/c) and to be significantly modified in A-A collisions (jet quenching). In this transverse momentum region, models incorporating purturbative QCD(pQCD)coupled with soft physics and energy loss [15] have demonstrated that fragmentation functions play an important role in hadron production [16]. The current results suggest that hard processed may also have a significant influence in the intermediate p_T region.

The antiparticle to particle ratios show no significant dependence on centrality. The values obtained in Cu+Cu are consistent within errors with those measured in Au+Au collisions at the same energy. The $\frac{K}{\pi}$ ratio shows a dependence on centrality at mid rapidity, but is found to be relatively constant at forward rapidity except for the most peripheral events The slight excess of $\frac{K^+}{\pi^+}$ over $\frac{K^-}{\pi^-}$ at mid rapidity and the much larger excess at forward rapidity may be due to the non-zero net baryon density which favors associated production of K^+ over K^-. An enhancement of baryons over mesons is observed at both rapidities in Cu+Cu as in Au+Au at the same energy. There appears to be a centrality dependence of the baryon to meson ratio with the ratio decreasing from central to peripheral collisions. This may be attributed to the decreasing suppression of the mesons with centrality.

While pQCD calculations underestimate the baryon to meson ratio by a large factor, the coalescence/recombination[8] mechanism and baryon junction transport[12] are found to describe well the measured baryon to meson ratio at mid-rapidity in the intermediate p_T region ($2 < p_T < 6$ GeV/c) in Au+Au collisions. The coalescence/recombination (ReCo) model assumes a thermalized flowing partonic medium with an exponential spectrum at smaller p_T and a spectrum of hard scattered partons described by parton fragmentation functions or power law functions dominating at higher p_T.

Understanding the underlying mechanisms responsible for hadron production over the whole range of transverse momentum and rapidity accessible at RHIC and providing a consistent description of all the various aspects of the hadron spectra in heavy ion collisions remains to be a major challenge of RHIC physics. The current data should help to constrain theoretical attempts to reach this synthesis.

V. ACKNOWLEDGEMENTS

This work was supported by the office of Nuclear Physics of the U.S. Department of energy, the Danish Natural Science Research Council, the Research Council of Norway, the Polish State Committee for Scientific Research (KBN), and the Romanian Ministry of Research.

[1] E. Laermann and O. Philipsen, hep-ph/0303042 (to appear in Ann. Rev. Nuc. Part. Sc.)

[2] BRAHMS,STAR,PHENIX,PHOBOS white papers.

$y=0$	$\frac{dN}{dy}$	$(\frac{dN}{dy})_m$	$(\frac{dN}{dy})_m/\frac{dN}{dy}$	$\frac{dN}{dy}$	$(\frac{dN}{dy})_m$	$(\frac{dN}{dy})_m/\frac{dN}{dy}$	$\langle p_T \rangle$
Cent.	π^-			π^+			
$0-10\%$	72.01 ± 2.35	47.27 ± 0.92	66%	72.96 ± 2.38	48.40 ± 0.95	66%	477.41 ± 7.61
$10-30\%$	40.26 ± 0.95	26.70 ± 0.43	66%	41.47 ± 0.98	28.08 ± 0.46	68%	479.06 ± 5.85
$30-50\%$	17.30 ± 0.18	11.82 ± 0.27	68%	18.04 ± 0.19	12.53 ± 0.29	69%	482.87 ± 4.18
$50-70\%$	6.18 ± 0.34	4.43 ± 0.18	72%	6.45 ± 0.36	4.67 ± 0.19	72%	484.33 ± 14.16
	K^-			K^+			
$0-10\%$	11.67 ± 0.60	8.04 ± 0.15	69%	12.82 ± 0.66	8.78 ± 0.17	68%	673.57 ± 9.66
$10-30\%$	6.65 ± 0.24	4.38 ± 0.07	66%	7.32 ± 0.27	4.91 ± 0.08	67%	656.21 ± 7.38
$30-50\%$	2.92 ± 0.04	1.79 ± 0.04	61%	3.22 ± 0.05	1.98 ± 0.05	61%	632.03 ± 5.25
$50-70\%$	0.89 ± 0.07	0.56 ± 0.03	62%	1.14 ± 0.09	0.70 ± 0.06	61%	608.53 ± 17.01
	$\bar{p}$			p			
$0-10\%$	5.84 ± 0.45	4.63 ± 0.08	79%	7.75 ± 0.60	6.15 ± 0.11	79%	947.97 ± 12.25
$10-30\%$	3.46 ± 0.19	2.62 ± 0.04	76%	4.54 ± 0.24	3.46 ± 0.05	76%	903.76 ± 9.52
$30-50\%$	1.56 ± 0.03	1.13 ± 0.02	72%	2.13 ± 0.04	1.54 ± 0.03	72%	839.60 ± 6.59
$50-70\%$	0.60 ± 0.07	0.42 ± 0.02	70%	0.74 ± 0.09	0.51 ± 0.02	69%	778.78 ± 22.14

TABLE II. Results at y = 0 extracted from simultaneous blast wave fits for pions, kaons, (anti)protons. The results are averages over six fit ranges.

$y=3$	$\frac{dN}{dy}$	$(\frac{dN}{dy})_m$	$(\frac{dN}{dy})_m/\frac{dN}{dy}$	$\frac{dN}{dy}$	$(\frac{dN}{dy})_m$	$(\frac{dN}{dy})_m/\frac{dN}{dy}$	$\langle p_T \rangle$
Cent.	π^-			π^+			
$0-10\%$	29.18 ± 0.92	12.24 ± 0.67	42%	28.38 ± 0.89	9.54 ± 0.17	34%	437.71 ± 6.93
$10-30\%$	17.34 ± 0.28	8.62 ± 0.44	50%	15.71 ± 0.25	5.56 ± 0.08	35%	462.04 ± 3.87
$30-50\%$	8.75 ± 0.24	3.89 ± 0.28	44%	7.89 ± 0.21	2.60 ± 0.06	33%	442.15 ± 6.06
$50-70\%$	3.01 ± 0.10	1.47 ± 0.18	49%	2.72 ± 0.09	1.00 ± 0.04	37%	468.92 ± 7.81
	K^-			K^+			
$0-10\%$	3.92 ± 0.19	1.15 ± 0.03	29%	5.40 ± 0.27	1.57 ± 0.03	29%	568.97 ± 8.59
$10-30\%$	2.35 ± 0.06	0.69 ± 0.01	29%	3.39 ± 0.08	0.98 ± 0.02	29%	570.32 ± 4.51
$30-50\%$	1.06 ± 0.04	0.28 ± 0.01	27%	1.60 ± 0.07	0.42 ± 0.01	26%	547.64 ± 7.18
$50-70\%$	0.37 ± 0.02	0.10 ± 0.01	27%	0.47 ± 0.02	0.13 ± 0.01	27%	553.74 ± 8.74
	$\bar{p}$			p			
$0-10\%$	1.13 ± 0.09	0.79 ± 0.02	70%	7.22 ± 0.55	5.51 ± 0.04	76%	765.14 ± 12.32
$10-30\%$	0.85 ± 0.03	0.58 ± 0.01	69%	4.63 ± 0.16	3.40 ± 0.02	74%	736.96 ± 6.10
$30-50\%$	0.38 ± 0.02	0.25 ± 0.01	66%	2.10 ± 0.13	1.53 ± 0.02	73%	707.30 ± 9.99
$50-70\%$	0.15 ± 0.01	0.10 ± 0.01	65%	0.82 ± 0.06	0.61 ± 0.01	74%	687.20 ± 11.42

TABLE III. Results at y = 3 extracted from simultaneous blast wave fits for pions, kaons, (anti)protons. The results are averages over six fit ranges.

[3] M. Adamczyk *et al.* (BRAHMS Collaboration), Nucl. Instrum. Meth., A**499**, (2003) 437.

[4] C. Adler *et al.* (STAR COLLABORATION), Phys. Rev. Lett. **89** (2002) 092301

[5] K. Adox *et al.* (PHENIX COLLABORATION), Phys. Rev. Lett. **89** (2002) 092302

[6] B. Tomasik, U. A. Wiedemann and U. W. Heinz, Heavy Ion Phys. **17**, 105 (2003) [nucl-th/9907096].

[7] Need hadron suppression references from BRAHMS,STAR,PHENIX

[8] V. Greco, C.M. Ko and P. Levai, Phys. Rev. Lett. **90** (2003) 202302 ; R.J. Fries, B. Muller, C. Nonoka and S.A. Bass, Phys. Rev. Lett. **90** (2003) 202303; V. Creco, C.M. Ko and I. Vitev, Phys. Rev. C **71** (2005)041901

[9] T. Hirano and Y. Nara, nucl-th/0404039v3

[10] Need GLV reference

$y=0$	π^- (p_T Exp.)				π^+ (p_T Exp.)			
Cent.	$\frac{dN}{dy}$	T	$\langle p_T \rangle$	$\frac{\chi^2}{d.o.f}$	$\frac{dN}{dy}$	T	$\langle p_T \rangle$	$\frac{\chi^2}{d.o.f}$
$0-10\%$	68.3 ± 2.8	242.3 ± 4.6	484.6 ± 9.3	7.2/7	71.3 ± 2.9	238.3 ± 4.5	476.6 ± 9.1	7.8/7
$10-30\%$	38.3 ± 1.4	241.7 ± 4.3	483.5 ± 8.7	11.6/7	40.4 ± 1.5	238.7 ± 4.2	477.4 ± 8.5	12.2/7
$30-50\%$	17.0 ± 0.8	238.2 ± 5.0	476.4 ± 10.0	8.8/7	18.2 ± 0.8	235.4 ± 4.9	470.8 ± 9.8	8.7/7
$50-70\%$	6.41 ± 0.44	231.19 ± 7.05	462.38 ± 14.10	6.04/7	6.82 ± 0.47	229.25 ± 6.91	458.50 ± 13.83	6.03/7
	π^- (m_T Exp.)				π^+ (m_T Exp.)			
$0-10\%$	64.9 ± 2.5	239.2 ± 4.6	501.1 ± 9.0	8.6/7	67.6 ± 2.7	235.2 ± 4.5	493.4 ± 8.8	9.3/7
$10-30\%$	36.4 ± 1.3	238.7 ± 4.3	500.0 ± 8.4	13.5/7	38.3 ± 1.4	235.7 ± 4.2	494.3 ± 8.2	14.2/7
$30-50\%$	16.1 ± 0.7	235.1 ± 5.0	493.2 ± 9.7	10.3/7	17.3 ± 0.8	232.4 ± 4.9	487.9 ± 9.5	10.1/7
$50-70\%$	6.1 ± 0.4	228.3 ± 7.0	479.9 ± 13.7	6.9/7	6.4 ± 0.4	226.3 ± 6.9	476.0 ± 13.4	6.8/7
	π^- (*Power law*)				π^+ (*Powerlaw*)			
Cent.	$\frac{dN}{dy}$	n	$\langle p_T \rangle$	$\frac{\chi^2}{d.o.f}$	$\frac{dN}{dy}$	n	$\langle p_T \rangle$	$\frac{\chi^2}{d.o.f}$
$0-10\%$	80.28 ± 8.53	15.63 ± 4.56	449.33 ± 21.95	0.34/7	87.86 ± 10.10	13.39 ± 3.29	432.06 ± 22.89	0.12/7
$10-30\%$	45.47 ± 4.59	14.62 ± 3.69	446.44 ± 20.78	1.30/7	50.38 ± 5.48	12.90 ± 2.83	430.28 ± 21.67	0.47/7
$30-50\%$	21.77 ± 2.97	11.59 ± 2.76	424.15 ± 26.92	0.26/7	23.33 ± 3.17	12.18 ± 2.97	418.80 ± 26.31	0.09/7
$50-70\%$	8.51 ± 1.83	11.10 ± 3.58	403.78 ± 40.36	0.14/7	9.09 ± 1.94	11.16 ± 3.52	399.47 ± 39.28	0.83/7
$y=3$	π^- (p_T Exp.)				π^+ (p_T Exp.)			
Cent.	$\frac{dN}{dy}$	T	$\langle p_T \rangle$	$\frac{\chi^2}{d.o.f}$	$\frac{dN}{dy}$	T	$\langle p_T \rangle$	$\frac{\chi^2}{d.o.f}$
$0-10\%$	28.18 ± 1.22	217.53 ± 3.58	435.07 ± 7.17	4.28/7	27.75 ± 1.37	216.10 ± 3.99	432.21 ± 7.97	17.32/7
$10-30\%$	18.45 ± 0.77	219.63 ± 3.47	439.26 ± 6.94	4.44/7	15.71 ± 0.69	225.86 ± 3.97	451.73 ± 7.94	8.91/7
$30-50\%$	9.04 ± 0.46	212.23 ± 4.06	424.47 ± 8.11	14.13/7	7.62 ± 0.42	217.74 ± 4.58	435.48 ± 9.16	9.27/7
$50-70\%$	3.21 ± 0.22	220.48 ± 6.08	440.96 ± 12.16	7.65/7	3.00 ± 0.23	215.94 ± 6.22	431.88 ± 12.45	19.36/7
	π^- (m_T Exp.)				π^+ (m_T Exp.)			
$0-10\%$	26.31 ± 1.09	214.98 ± 3.57	453.99 ± 6.93	4.50/7	25.84 ± 1.22	213.67 ± 3.97	451.46 ± 7.74	18.53/7
$10-30\%$	17.25 ± 0.68	217.09 ± 3.45	458.10 ± 6.71	4.86/7	14.74 ± 0.62	223.29 ± 3.96	470.16 ± 7.69	9.76/7
$30-50\%$	8.41 ± 0.41	209.72 ± 4.04	443.75 ± 7.86	14.89/7	7.10 ± 0.37	215.27 ± 4.57	454.57 ± 8.89	10.15/7
$50-70\%$	3.00 ± 0.20	217.95 ± 6.06	459.76 ± 11.77	8.09/7	2.81 ± 0.20	213.28 ± 6.19	450.70 ± 12.04	19.17/7
	π^- (*Power law*)				π^+ (*Powerlaw*)			
Cent.	$\frac{dN}{dy}$	n	$\langle p_T \rangle$	$\frac{\chi^2}{d.o.f}$	$\frac{dN}{dy}$	n	$\langle p_T \rangle$	$\frac{\chi^2}{d.o.f}$
$0-10\%$	37.07 ± 3.19	17.44 ± 2.80	381.77 ± 13.82	15.53/8	40.32 ± 4.17	16.18 ± 2.44	365.56 ± 15.50	9.47/8
$10-30\%$	22.56 ± 1.68	22.69 ± 4.45	397.71 ± 12.36	18.13/8	19.76 ± 1.57	20.93 ± 4.02	403.38 ± 13.43	20.50/8
$30-50\%$	12.79 ± 1.37	15.63 ± 2.47	361.58 ± 15.99	18.29/8	10.46 ± 1.15	16.63 ± 2.98	376.53 ± 17.09	8.45/8
$50-70\%$	3.98 ± 0.52	21.23 ± 6.90	400.30 ± 21.71	5.61/8	4.02 ± 0.60	16.46 ± 4.22	379.79 ± 23.49	19.86/8

TABLE IV. Extracted fit results for pions. The fit range is $0.4 < p_T < 1.6$ GeV/c for the exponential fits and $0.5 < p_T < 2.0$ GeV/c for the power law fits

[11] P. Levai, G. Papp, G. Fai and M. Guylassy, nucl-th/0012017v2

[12] I. Vitev and M. Gyulassy, Phys. Rev. C **65** (2002) 041902 (R); Nucl. Phys. A **715** (2003) 779c;V. Topor Pop, M. Gyulassy et al, Phys. Rev. C**68** (2003) 054902

[13] X. F. Guo and X. N. Wang, Phys. Rev. Lett. **85**, 3591 (2000); Nucl. Phys. A**696**, 788 (2001)

[14] R.C. Hwa and C. B. Yang, Phys. Rev. C**70** (2004) 024905; R. J. Fries *et. al*, arXiv:nucl-ex/0601042v1

[15] I. Vitev and M. Gyulassy, Phys. Rev. C**65** (2002) 041902

[16] X. Zang, G. Fai and P. Levai, Phys. Rev. Lett. **89** (2002) 272301

[17] L.V. Gribov, E. M. Levin, M.G.Ryskin, Phys. Rep. 100 (1983) 1

[18] D. Kharzeev, E. Levin, L. McLerran, Phys. Lett. B 561 (2003) 93

[19] P. Huovinen, P.F. Kolb, U. Heinz, P.V. Ruuskanen and S.A. Voloshin, Phys. Lett. B**503**, 58 (2001), T. Hirano and Y. Nara, Phys. Rev. C**69** (2004) 034908

$y=0$	K^- (p_T *Exp.*)				K^+ (p_T *Exp.*)			
Cent.	$\frac{dN}{dy}$	T	$\langle p_T \rangle$	$\frac{\chi^2}{d.o.f}$	$\frac{dN}{dy}$	T	$\langle p_T \rangle$	$\frac{\chi^2}{d.o.f}$
$0-10\%$	12.54 ± 0.40	321.72 ± 7.51	643.45 ± 15.02	4.02/7	13.77 ± 0.45	317.79 ± 7.28	635.57 ± 14.56	5.88/7
$10-30\%$	6.85 ± 0.20	318.19 ± 6.82	636.38 ± 13.65	4.94/7	7.81 ± 0.24	310.31 ± 6.57	620.61 ± 13.14	2.34/7
$30-50\%$	2.79 ± 0.10	315.33 ± 8.02	630.66 ± 16.04	12.34/7	3.11 ± 0.12	314.03 ± 8.16	628.07 ± 16.31	7.31/7
$50-70\%$	0.85 ± 0.05	317.90 ± 13.71	635.79 ± 27.41	6.40/7	1.21 ± 0.09	284.07 ± 11.89	568.13 ± 23.78	2.13/7
	K^- (m_T *Exp.*)				K^+ (m_T *Exp.*)			
$0-10\%$	11.23 ± 0.33	280.75 ± 6.92	682.18 ± 13.27	1.52/7	12.32 ± 0.37	277.33 ± 6.71	675.64 ± 12.86	1.24/7
$10-30\%$	6.12 ± 0.17	277.51 ± 6.30	675.97 ± 12.08	2.31/7	6.92 ± 0.19	271.26 ± 6.08	664.00 ± 11.66	0.81/7
$30-50\%$	2.50 ± 0.09	274.32 ± 7.37	669.87 ± 14.14	6.74/7	2.78 ± 0.10	273.71 ± 7.51	668.69 ± 14.40	2.86/7
$50-70\%$	0.75 ± 0.04	279.47 ± 12.56	679.74 ± 24.07	5.32/7	1.02 ± 0.07	251.68 ± 11.00	626.40 ± 21.14	1.81/7
	K^- (m_T *Boltz.*)				K^+ (m_T *Boltz.*)			
$0-10\%$	10.71 ± 0.31	222.29 ± 4.56	690.95 ± 12.59	3.90/7	11.75 ± 0.35	220.32 ± 4.44	685.55 ± 12.26	2.14/7
$10-30\%$	5.83 ± 0.16	220.17 ± 4.17	685.14 ± 11.51	5.68/7	6.59 ± 0.19	216.46 ± 4.06	674.96 ± 11.19	4.38/7
$30-50\%$	2.39 ± 0.08	218.11 ± 4.89	679.50 ± 13.49	6.58/7	2.65 ± 0.09	217.88 ± 4.99	678.86 ± 13.76	3.17/7
$50-70\%$	0.71 ± 0.04	222.20 ± 8.25	690.72 ± 22.79	5.41/7	0.96 ± 0.06	205.07 ± 7.58	643.78 ± 20.80	2.34/7
$y=3$	K^- (p_T *Exp.*)				K^+ (p_T *Exp.*)			
$0-10\%$	5.29 ± 0.38	242.01 ± 6.94	484.02 ± 13.88	8.31/4	5.85 ± 0.36	267.72 ± 7.79	535.44 ± 15.57	5.74/4
$10-30\%$	3.05 ± 0.21	246.01 ± 6.84	492.01 ± 13.69	6.00/4	3.88 ± 0.23	258.55 ± 6.75	517.11 ± 13.51	9.68/4
$30-50\%$	1.53 ± 0.15	225.22 ± 8.03	450.45 ± 16.06	2.55/4	1.79 ± 0.14	249.40 ± 8.09	498.80 ± 16.18	8.21/4
$50-70\%$	0.44 ± 0.06	250.40 ± 16.10	500.80 ± 32.21	1.69/4	0.50 ± 0.07	261.60 ± 16.66	523.19 ± 33.32	5.64/4
	K^- (m_T *Exp.*)				K^+ (m_T *Exp.*)			
$0-10\%$	3.75 ± 0.19	227.65 ± 4.64	580.16 ± 8.95	12.55/6	4.45 ± 0.19	249.75 ± 4.72	622.69 ± 9.07	8.01/6
$10-30\%$	2.18 ± 0.10	231.53 ± 4.48	587.64 ± 8.63	7.70/6	2.86 ± 0.12	244.89 ± 4.33	613.35 ± 8.33	11.19/6
$30-50\%$	0.97 ± 0.07	220.29 ± 6.13	565.95 ± 11.83	12.47/6	1.26 ± 0.07	239.66 ± 5.54	603.29 ± 10.67	12.99/6
$50-70\%$	0.34 ± 0.03	220.40 ± 9.27	566.18 ± 17.90	1.93/6	0.39 ± 0.03	239.58 ± 9.58	603.14 ± 18.44	6.51/6
	K^- (m_T *Boltz.*)				K^+ (m_T *Boltz.*)			
$0-10\%$	3.31 ± 0.17	193.93 ± 3.48	613.34 ± 9.51	14.42/6	3.95 ± 0.17	210.39 ± 3.46	658.34 ± 9.52	10.76/6
$10-30\%$	1.93 ± 0.09	196.94 ± 3.36	621.57 ± 9.19	10.15/6	2.54 ± 0.11	206.77 ± 3.20	648.43 ± 8.77	13.61/6
$30-50\%$	0.86 ± 0.06	188.05 ± 4.64	597.33 ± 13.12	15.62/6	1.12 ± 0.06	202.58 ± 4.10	636.96 ± 11.24	15.47/6
$50-70\%$	0.30 ± 0.03	188.86 ± 7.03	599.54 ± 19.58	1.44/6	0.34 ± 0.03	203.19 ± 7.12	638.64 ± 19.51	6.72/6

TABLE V. Extracted fit results for kaons. The fit range is $0.4 < p_T < 1.6$ GeV/c at y=0 and $0.7 < p_T < 1.6$ GeV/c at y=3

[20] J.C. Collines and D. E. Soper, Nucl. Phys. B**194**, 445 1982

[21] F. Karsch, Z. Phys. C**38**, 147 (1988); F. Karsch, hep-lat/0106019.

[22] G. Agakishiev *et al.* [STAR Collaboration], Phys. Rev. Lett. **108**, 072301 (2012) [arXiv:1107.2955 [nucl-ex]].

$y = 0$	$\bar{p}$ (m_T *Exp.*)				p (m_T *Exp.*)			
Cent.	$\frac{dN}{dy}$	T	$\langle p_T \rangle$	$\frac{\chi^2}{d.o.f}$	$\frac{dN}{dy}$	T	$\langle p_T \rangle$	$\frac{\chi^2}{d.o.f}$
$0-10\%$	6.06 ± 0.15	345.34 ± 7.79	933.31 ± 15.21	$10.46/8$	8.14 ± 0.20	335.05 ± 7.41	913.19 ± 14.51	$6.69/8$
$10-30\%$	3.52 ± 0.08	324.05 ± 6.56	891.61 ± 12.87	$3.47/8$	4.67 ± 0.11	317.10 ± 6.32	877.96 ± 12.44	$1.19/8$
$30-50\%$	1.55 ± 0.05	296.35 ± 7.07	837.01 ± 13.99	$4.49/8$	2.15 ± 0.07	288.39 ± 6.66	821.22 ± 13.22	$0.96/8$
$50-70\%$	0.59 ± 0.03	264.21 ± 9.47	773.01 ± 18.98	$4.90/8$	0.73 ± 0.04	260.59 ± 8.39	765.75 ± 16.85	$2.06/8$
	$\bar{p}$ (m_T *Boltz.*)				p (m_T *Boltz.*)			
$0-10\%$	5.96 ± 0.15	282.22 ± 5.31	923.45 ± 14.25	$6.38/8$	8.01 ± 0.20	275.26 ± 5.12	906.38 ± 13.70	$3.79/8$
$10-30\%$	3.45 ± 0.08	267.90 ± 4.59	888.10 ± 12.27	$1.84/8$	4.59 ± 0.11	263.03 ± 4.46	875.89 ± 11.90	$0.57/8$
$30-50\%$	1.52 ± 0.05	248.69 ± 5.11	839.52 ± 13.62	$5.55/8$	2.10 ± 0.06	242.94 ± 4.85	824.79 ± 12.92	$2.43/8$
$50-70\%$	0.58 ± 0.03	225.64 ± 7.10	779.98 ± 18.87	$6.48/8$	0.72 ± 0.04	223.12 ± 6.31	773.42 ± 16.77	$2.40/8$
$y = 3$	$\bar{p}$ (m_T *Exp.*)				p (m_T *Exp.*)			
$0-10\%$	1.19 ± 0.04	248.09 ± 4.60	740.58 ± 9.29	$10.37/8$	7.09 ± 0.15	263.20 ± 3.50	770.97 ± 7.02	$12.52/8$
$10-30\%$	0.88 ± 0.03	238.11 ± 4.29	720.35 ± 8.71	$16.73/8$	4.39 ± 0.09	254.85 ± 3.32	754.21 ± 6.68	$12.78/8$
$30-50\%$	0.38 ± 0.01	231.51 ± 5.24	706.92 ± 10.70	$12.13/8$	1.96 ± 0.04	242.21 ± 3.36	728.67 ± 6.81	$20.28/8$
$50-70\%$	0.15 ± 0.01	217.23 ± 7.91	677.66 ± 16.27	$18.39/8$	0.77 ± 0.02	229.66 ± 3.88	703.15 ± 7.93	$23.67/8$
	$\bar{p}$ (m_T *Boltz.*)				p (m_T *Boltz.*)			
$0-10\%$	1.16 ± 0.04	213.98 ± 3.51	749.50 ± 9.34	$12.25/8$	6.94 ± 0.14	224.84 ± 2.62	777.91 ± 6.97	$14.89/8$
$10-30\%$	0.86 ± 0.03	206.41 ± 3.31	729.62 ± 8.81	$22.16/8$	4.30 ± 0.09	218.63 ± 2.51	761.68 ± 6.67	$17.20/8$
$30-50\%$	0.36 ± 0.01	201.41 ± 4.08	716.44 ± 10.84	$15.46/8$	1.91 ± 0.04	209.29 ± 2.58	737.19 ± 6.87	$29.05/8$
$50-70\%$	0.15 ± 0.01	190.45 ± 6.29	687.50 ± 17.01	$20.07/8$	0.75 ± 0.02	199.53 ± 3.02	711.48 ± 8.04	$31.58/8$

TABLE VI. Extracted fit results for protons and anti-protons. The fit range is $0.5 < p_T < 2.0$ GeV/c.